Interstitial photodynamic therapy for primary prostate cancer incorporating realtime treatment dosimetry

Johansson, Ann; Axelsson, Johan; Swartling, Johannes; Johansson, Thomas; Palsson, Sara; Stensson, Johan; Einarsdottir, Margret; Svanberg, Katarina; Bendsöe, Niels; Kalkner, Karl Mikael; Nilsson, Sten; Svanberg, Sune; Andersson-Engels, Stefan

Published in:
Progress in Biomedical Optics and Imaging - Proceedings of SPIE

DOI:
10.1117/12.699903

2007

Interstitial photodynamic therapy for primary prostate cancer incorporating realtime treatment dosimetry

Ann Johansson[a], Johan Axelsson[a], Johannes Swartling[b], Thomas Johansson[b], Sara Pålsson[b], Johan Stensson[b], Margret Einarsdóttír[c], Katarina Svanberg[c], Niels Bendsoe[d], Karl Mikael Kälkner[e], Sten Nilsson[e], Sune Svanberg[a], Stefan Andersson-Engels[a]

[a]Lund University, Department of Physics, PO Box 118, SE-221 00 Lund, Sweden;
[b]SpectraCure AB, Ole Römers väg 16, SE-223 70 Lund, Sweden;
[c]Lund University Hospital, Department of Oncology, SE-221 85 Lund, Sweden;
[d]Lund University Hospital, Department of Dermatology, SE-221 85, Lund, Sweden;
[e]Karolinska University Hospital, Department of Oncology and Pathology, Stockholm, Sweden

ABSTRACT

Photodynamic therapy (PDT) for the treatment of prostate cancer has been demonstrated to be a safe treatment option capable of inducing tissue necrosis and decrease in prostate specific antigen (PSA). Research groups report on large variations in treatment response, possibly due to biological variations in tissue composition and short-term response to the therapeutic irradiation. Within our group, an instrument for interstitial PDT on prostate tissue that incorporates realtime treatment feedback is being developed. The treatment protocol consists of two parts. The first part incorporates the pre-treatment plan with ultrasound investigations, providing the geometry for the prostate gland and surrounding risk organs, an iterative random-search algorithm to determine near-optimal fiber positions within the reconstructed geometry and a Block-Cimmino optimization algorithm for predicting individual fiber irradiation times. During the second part, the therapeutic light delivery is combined with measurements of the light transmission signals between the optical fibers, thus monitoring the tissue effective attenuation coefficient by means of spatially resolved spectroscopy. These data are then used as input for repeated runs of the Block-Cimmino optimization algorithm. Thus, the irradiation times for individual fibers are updated throughout the treatment in order to compensate for the influence of changes in tissue composition on the light distribution at the therapeutic wavelength.

Keywords: photodynamic therapy, prostate cancer, interstitial, dosimetry, fluorescence spectroscopy, absorption spectroscopy

1. INTRODUCTION

Photodynamic therapy (PDT) has become a clinically more accepted method for treating certain types of malignancies in various organs, partly due to advantages such as the possibility of repeated treatment and restriction of the treatment-induced tissue damage to irradiated sites. The PDT effect is caused by a combination of treatment induced apoptosis and direct necrosis,[1] vascular damage[2] and possibly an elicited immune response,[3] where the extent of tissue damage depends on the light dose, the tissue oxygenation and the sensitizer concentration.[4] For PDT, clinical treatment protocols often rely on a light dose threshold model. This simplified model is based on the assumption that only tissue regions exposed to a light dose exceeding a pre-defined threshold are damaged.[5] The threshold light dose is likely to depend on tissue type and photosensitizer used.[6] From the point of view of the deposited light dose, information on the tissue optical properties is important. Significant inter- and intra-patient variations of the absorption and scattering coefficients of prostate tissue have been measured by many groups.[7–9] In addition, any treatment-induced variations in absorption and scattering, possibly due to changes in blood content and tissue oxygenation status, directly influence the light distribution during the course of the treatment.[10] Clearly, there is a need to monitor the tissue optical properties in individual patients both before

Further author information: email: ann.johansson@fysik.lth.se, tel: +46 462223120

Optical Methods for Tumor Treatment and Detection: Mechanisms and Techniques in Photodynamic Therapy XVI, edited by David Kessel, Proc. of SPIE Vol. 6427, 64270O, (2007) · 1605-7422/07/$18 · doi: 10.1117/12.699903

and during the treatment.

Recently, several groups have proved PDT a successful alternative for the treatment of prostate cancer.[11] Bown *et al.* have used the photosensitizer mTHPC for treating secondary and primary prostate cancer.[12,13] Weersink *et al.* have reported on treatment of recurrent prostate cancer using the vascular-targeted photosensitizer Tookad, (WST09),[8,14] whereas Du *et al.* have utilized the photosensitizer Motexafin Lutetium for the treatment of recurrent prostate carcinoma.[15] In common for the different PDT-trials on prostate tissue were the large intra- and inter-patient variations in treatment-induced necrotic volumes despite delivering similar drug and light doses. These variations can possibly be due to biological differences in tissue composition and short-term treatment response, directly influencing the light distribution within the prostate tissue.

In order to overcome some of the difficulties associated with treatment dosimetry for interstitial PDT (IPDT) we have developed instrumentation that utilizes 6-18 thin optical fibers for therapeutic light delivery. The same fibers can be used for realtime monitoring of tissue optical properties, sensitizer concentration and tissue oxygen saturation during the course of the treatment.[10,16] Previously, we have reported on significant treatment-induced changes in tissue optical properties during IPDT of thick skin tumors.[10] The conclusions from this work were that there is a need for treatment feedback, possibly based on the measured light transmission signals, to compensate the influence of varying light transmission on the deposited light dose within tumors.[17] Our most recent IPDT instrumentation therefore incorporates realtime monitoring of and treatment feedback based on the light transmission between the treatment fibers. The idea is to allow the observed changes in light transmission to influence the energy delivered via each individual fiber, thereby ascertaining a certain pre-determined light dose to the target tissue.

Here we report on algorithms constituting a dosimetry module for IPDT on prostate tissue with realtime treatment feedback based on a light dose threshold model. The algorithms have been developed to execute on a novel 18-fiber IPDT instrument and incorporate pre-treatment planning as well as modules for updating the treatment parameters during the PDT procedure. More specifically, the pre-treatment planning module incorporates algorithms for reconstruction of the full three-dimensional target geometry from a set of ultrasound images, optimization of the fiber positions within this geometry and estimation of individual fiber irradiation times. During the IPDT treatment session, the algorithms that execute, referred to as the realtime dosimetry module, utilize data on light transmission between optical fibers to evaluate possible treatment-induced changes of the light attenuation coefficient. A Cimmino optimization algorithm is then used for calculating individual fiber irradiation times. The light dose delivered via each fiber can thus be updated throughout the treatment session to accommodate any treatment-induced changes in tissue light transmission. The Cimmino algorithm is set to optimize the light dose within the target tissue, i.e. the prostate glandular tissue, while minimizing the dose to the surrounding risk organs, such as the urethra, rectum, upper and lower sphincters and the cavernous nerve bundles. A finite element method (FEM) is utilized in order to simulate light transmission signals within a realistic prostate model for temporally and spatially varying tissue optical properties. The resulting dose volume histograms (DVHs) of the delivered light dose for these simulated IPDT treatments are compared with and without treatment feedback. In this way, we demonstrate the feasibility of an IPDT dosimetry model that ascertains a certain pre-determined light dose within the target tissue irrespective of any treatment-induced changes in tissue absorption.

2. METHODS AND ALGORITHMS

The entire treatment procedure, also indicating what steps are included within the pre-treatment or the realtime treatment dosimetry modules, is illustrated as a flow chart in Fig. 1. In this section, we begin by giving an overview of the treatment procedure, whereas sections 2.1-2.4 describe the individual dosimetry modules in more detail. Section 2.5 describes how the light distribution within a realistic prostate geometry is modeled for different sets of tissue optical properties. The modeled data thus provide input for the realtime dosimetry module. Based on the simulated data sets, we evaluate the concept of spatially resolved spectroscopy to monitor the light attenuation within the prostate and test the concept of realtime treatment feedback via measured light transmission signals.

At first, an ultrasound investigation of the prostate is performed to assess the glandular volume as well as the geometry of the tissue region (step 1). Within a set of ultrasound images, the extent of the prostatic gland, urethra, rectum, upper and lower sphincters and the cavernous nerve bundles is delineated by the urologist. The different tissue contours within each ultrasound image are then patched into a full three-dimensional geometry for all organ types (step 2). The patient is thereafter prepared for surgery, providing a time window for a random-search algorithm to calculate the near-optimal fiber positions within the reconstructed geometry (step 3). The optical fibers, also referred to as treatment fibers, are guided into position utilizing hollow steel needles (step 4). Within this fourth step, the urologist stores the final fiber positions as they might deviate slightly from the outcome of step 3. Information on the geometry and the actual fiber positions is used as input for a Cimmino optimization algorithm that is executed to predict individual fiber irradiation times (step 5). Steps 1-5 in Fig. 1 constitute what is here referred to as the pre-treatment dosimetry module. Hereafter, the pre-treatment planning ends and the IPDT session begins. The treatment procedure involves continuous iterations of measurement (step 6) and treatment (step 7) sequences. The measurement sequences involve monitoring of the light transmission between the treatment fibers to detect any temporal and spatial variations of the light attenuation at the therapeutic wavelength. By means of spatially resolved spectroscopy, the effective attenuation coefficient is evaluated within different volumetric subsets of the prostate (step 8). In case significant variations are found, this information is used as input for a repeated run of the Cimmino optimization algorithm in order to update the irradiation times required to treat the entire prostatic gland (step 9). During the treatment sequences, light at the therapeutic wavelength is delivered for the time periods predicted by the Cimmino algorithm. Treatment and measurement sequences are iterated until a light dose exceeding the pre-defined threshold dose has been delivered to the prostate tissue. Steps 6-9 in Fig. 1 thus constitute the realtime treatment dosimetry module.

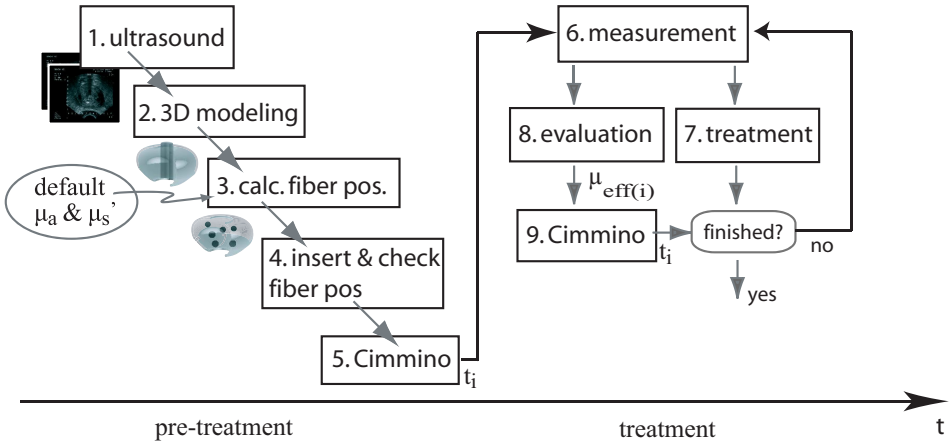

Figure 1. Flow chart illustrating the pre-treatment planning (steps 1-5) as well as the realtime dosimetry module (steps 6-9).

2.1. Geometry

The geometry model is a three-dimensional voxel representation of the prostate, as the target organ, and urethra, rectum, upper and lower sphincters and the cavernous nerve bundles, as risk organs. Within 6-10 ultrasound images, the physician marks 5-20 points delineating the periphery of the different tissue types present in that particular cross-section. These points are then connected by linear interpolation to form connected organ contours. From the ultrasound investigation, the transversal images are craniocaudally separated by 5 mm. The tissue contours are linearly interpolated to regions in between ultrasound cross-sections, giving voxel side lengths of 1 mm in all three dimensions. A simple filling technique is applied to specify the tissue type for voxels within the delineated contours; first, the center of each set of contour points is calculated. For each tissue type, the following procedure is executed; first, the center point of the current tissue type is put in a buffer. The first point in the buffer is then extracted and set to the same tissue type as the current tissue type. Thereafter its six

connected neighbors are tested for tissue type. If a point does not belong to the same tissue type as the current contour point and does not belong to another set of contour points it is put into the buffer. This procedure is repeated until the buffer is empty, thus filling every tissue type from its center and outwards. By applying the filling process of the different tissue types in the order *upper sphincter, lower sphincter, rectum, prostate and urethra*, the smaller organs, such as the urethra, can be correctly inscribed within the surrounding prostate. The reconstructed organs are inscribed within a block representing normal, surrounding tissue, resulting in a three-dimensional voxel model with a typical side length of 60-65 voxels.

2.2. Fiber positions

The problem of finding the optimal fiber positions can be formulated as maximizing the light fluence rate within the prostatic gland while minimizing the light distribution within the organs at risk (OAR). The optimization algorithm is an iterative random-search algorithm similar to a simulated annealing type algorithm. The search for optimal fiber positions is initialized by creating a random configuration of source positions within the prostate. The bare-ended fibers are modeled as isotropic point sources where the fluence rate in voxel j due to a source in voxel i, ϕ_{ij}, is approximated by the analytical solution to the diffusion equation within an infinite, homogeneous medium;

$$\phi_{ij} = \frac{P\,\mu_{\text{eff}}^2}{4\pi\mu_a r_{ij}}\,\exp\left(-\mu_{\text{eff}} r_{ij}\right). \tag{1}$$

P denotes the source strength, set to 0.15 W in this work, and the effective attenuation coefficient is given by $\mu_{\text{eff}} = [3\mu_a(\mu_a + \mu_s')]^{1/2}$, where μ_a and μ_s' were set to 0.5 and 9.7 cm^{-1}, respectively.[9] For every iteration, each fiber is moved a limited length in a random direction. The movement is restricted to voxels within the prostate and only one source fiber per voxel is allowed. Following a fiber movement, a fitness value is computed to evaluate the quality of the configuration:

$$F = \sum_{j=1}^{M} w_j^{\text{target}} \phi_{ij} + \sum_{j=1}^{N} w_j^{\text{OAR}} \phi_{ij} \tag{2}$$

The first summation includes a certain fraction of the prostate voxels with the lowest fluence rate. The target tissue weights, w_{ij}^{target}, are positive, contributing constructively to the fitness value when delivering light to this particular region. Correspondingly, the second summation includes voxels within the OAR, i.e. the urethra, rectum, upper and lower sphincters and the cavernous nerve bundles, characterized by the highest fluence rate. The corresponding tissue weights are negative, thereby causing any fluence rate within the OAR to punish the overall fitness function value. Eq. (2) thus seeks to maximize the lowest fluence rate values in the prostate while minimizing the highest fluence rate values outside the target tissue. For the iterative scheme, the new fiber positions are accepted only if a fiber movement leads to a higher fitness function value. As the light distribution can be considered diffuse at the earliest a distance $1/\mu_s'$ from the fiber tip, the resulting fiber positions are presented with the depth coordinate decreased by this distance.

Random-search algorithms of this type are not guaranteed to find the global optimum. However, the stochastic movements increases the probability that the search may find its way out of a local optimum. In the current implementation, the maximum step size is decreased gradually from three to one voxel to ensure that the solution will converge to an optimum, although this is at the expense of the ability to circumvent local optima. Typical execution times are on the order of 45 to 60 minutes.

2.3. Cimmino

The Cimmino optimization algorithm has been used for radiation therapy treatment planning[18] and also very recently for determination of light diffuser positions, lengths and strengths in prostate IPDT treatment planning.[19] Here we employ the Cimmino optimization algorithm[20] for the inverse problem of finding individual irradiation times, t_i, for I isotropic point sources. The algorithm accepts information on the tissue optical properties and the tissue geometry to calculate irradiation times for each treatment fiber. The optimization conditions can be expressed as the requirement to deliver a light dose exceeding a pre-determined threshold dose to the target tissue, while minimizing the dose to the surrounding sensitive tissues. The optimization problem can thus be

formulated as satisfying the following system of inequalities for the fluence, i.e. the fluence rate (ϕ) multiplied by the irradiation time (t), in all tissue voxels;

$$L_j \leq \langle \phi_j, t \rangle = \sum_{i=1}^{I} \phi_{ij} t_i \leq U_j \qquad j = 1, 2, ..., J$$
$$t_i \geq 0 \qquad i = 1, 2, ..., I \tag{3}$$

Here, ϕ_{ij}, denotes the fluence rate in voxel j due to point source i and L_j and U_j represent tissue type specific lower and upper limits for the delivered fluence, respectively. For the target tissue, L_j is set to 5 J/cm^2 and U_j to ∞ J/cm^2, whereas within OAR these thresholds are 0 and 5, respectively. ϕ_{ij} is given by Eq. (1), where each source fiber is characterized by a specific $\mu_{\text{eff}(i)}$, see section 2.4. For the first run of the Cimmino algorithm, step 5 in Fig. 1, a set of default prostate optical properties are utilized, where $\mu_{\text{eff}(i)} = 3.9$ cm^{-1} and $\mu_a = 0.5$ cm^{-1}. Once a measurement sequence has been performed, step 9 may update the prostate effective attenuation coefficient. The current implementation allows a different $\mu_{\text{eff}(i)}$ for each source fiber, thereby allowing some degree of spatial variation of this coefficient.

Each set of inequalities in Eq. (3) defines a hyperslab in the positive 2^J-tant in the J-dimensional space. A point lying within the hyperslab of every inequality would constitute a feasible solution but due to the large number of tissue voxels included in the problem, most often no feasible solution exists. Although not every constraint can be satisfied, the Cimmino optimization algorithm converges to a close approximation of the least-intensity feasible solution. The algorithm is based on an iterative scheme, starting from an arbitrary point in I-dimensional space, which is first projected orthogonally onto the first hyperslab. The resulting point is then projected onto the next hyperslab and so on. Non-violated constraints do not affect the new iteration, whereas voxels experiencing light doses outside the specified range bring the successive iteration closer to the optimal solution defined by Eq. (3). Iterations are stopped either when the solution has converged or when a stipulated maximum number of iterations has been reached. Each tissue type is associated with a certain weight, which reflects the relative importance associated with delivering a light dose outside the allowed interval. These weights can be adjusted to meet certain criteria on the resulting dose volume histogram of the delivered light dose. Dose volume histograms (DVHs) provide information on the fractional volume of the tissue of interest that receives a certain treatment dose and have been used in radiation treatment planning.[21] In this work, the requirements on the DVHs state that a light dose exceeding 5 J/cm^2 should be delivered to a minimum of 95% of the prostate tissue, while a maximum of 80% of the urethra and upper sphincter volumes are allowed this light dose. A slightly more restrictive requirement on the lower sphincter including the cavernous nerve bundles allows a maximum of 50% of this tissue type to be exposed to 75% of the 5 J/cm^2 light dose. These tissue weights are thus different in magnitude than the ones used in the optimization of the fiber positions. The ability of the Cimmino algorithm to fulfill the above criteria are checked by studying the resulting dose volume histograms (DVHs) of the delivered light dose. Details on this procedure will be part of a future publication.

2.4. Evaluation

The evaluation module utilizes data on the light transmission between treatment fibers to assess the spatially varying effective attenuation coefficient within the prostate volume. During a measurement sequence, each of the 18 treatment fibers sequentially emit light at the therapeutic wavelength. The light transmission signals to the six nearest neighboring fibers, placed at different distances, r_{ij}, from the source, are monitored. Here, indices i and j denote source and detector fibers, respectively. Assuming an infinite homogeneous medium, the light distribution can be described by Eq. (1). This equation can be re-written to yield;

$$-ln(\phi_{ij} r_{ij}) = -ln\left(\frac{P\,\mu_{\text{eff}(i)}^2}{4\pi\mu_a r_{ij}}\right) - \mu_{\text{eff}(i)} r_{ij} \qquad i = 1, 2, \ldots, 18 \qquad j = 1, 2, \ldots, 6 \tag{4}$$

The logarithm of the detected intensities multiplied with the source-detector distances is thus a first order polynomial with respect to r, where the slope equals the effective attenuation coefficient. A linear fit is performed 18 times, i.e. with each treatment fiber used as source fiber and the six closest fibers as detectors, resulting in 18 different coefficients, $\mu_{\text{eff}(i)}$. The procedure is similar to discretizing the entire gland into 18 sub-geometries

centered around the source fibers, where each sub-volume is characterized by a fiber specific light attenuation coefficient. Since no absolute measurements are performed, the absorption and scattering are not resolved separately.

Only transmission signals with a sufficiently high signal-to-noise-ratio (SNR) are used for evaluating $\mu_{\text{eff}(i)}$. Also, the source-detector separations must span a sufficiently large distance to allow a robust linear fit and the validity of Eq. (4). If all six transmission signals from a particular source fiber are characterized by sufficient SNR and source-detector separation, the linear fit is performed and the calculated effective attenuation coefficient is assigned to that source fiber. If the number of valid measurements is less than six, either due to noise rejection or too small source-detector distance, the transmission signals from more source fibers are combined and incorporated into the linear fit. This effectively expands the volume of the analyzed sub-geometry. If all measurements are subjected to rejections, $\mu_{\text{eff}(i)} = 3.9$ cm^{-1}.

2.5. Modeling of the light distribution, FEM

To provide realistic input for the realtime treatment dosimetry module, the finite element method (FEM) (Multiphysics® 3.1, Comsol AB, Stockholm, Sweden) was used to model the fluence rate distributions, $\phi(r)$, within a geometry model approximately representing the prostate, urethra, rectum and sphincters. The fluence rate was determined by solving the steady-state diffusion equation;

$$\nabla^2\phi(r) - \mu_{\text{eff}}^2\phi(r) = S_i \qquad i = 1, 2, \ldots, 18 \tag{5}$$

The bare-ended fibers, constituting the source terms, $S(r_i)$, were modeled as isotropic point sources at the calculated source fiber positions. Eq. (5) was solved with one source fiber active at a time resulting in the fluence rate in voxel j due to source i. For each simulation, the fluence rate at the positions of the six closest neighboring fibers was assessed, thus providing data on the light transmission between treatment fibers to be used as input for the *evaluation* module (step 8 in Fig. 1). The target and risk organs were inscribed within a tissue block, representing surrounding, normal tissue. Boundary conditions were expressed as;

$$\hat{n} \cdot \frac{\mu_a}{\mu_{\text{eff}}^2}\nabla\phi = 0 \tag{6}$$

.

3. RESULTS

Fig. 2.a is a schematic drawing of the organs incorporated into the geometry model, i.e. the target tissue, consisting of the prostate, and the OAR, consisting of the urethra, rectum, upper sphincter and lower sphincter also including the cavernous nerve bundles. Also outlined is the rectal ultrasound probe that is used to acquire the cross sections for reconstructing the geometry. Fig. 2.b shows the reconstructed geometry for a patient with a glandular volume of approximately 25 cm^3. The tissue peripheries had been outlined within 8 ultrasound images by an experienced urologist. Dark grey markers represent calculated fiber positions. For the results presented here, the fiber positioning algorithm was allowed 120 minutes execution time, resulting in a fitness value of 2.503. Varying the execution time between 45 and 120 minutes resulted in fitness values of 2.507($\pm$0.015) and no significant correlation between fitness value and total execution time could be observed ($P < 0.01$). Thus, calculation times limited to about one hour seem reasonable for the clinical situation.

The *evaluation* module was tested on light transmission data simulated by the FEM for five levels of homogeneous absorption within prostate tissue, $\mu_a = 0.5, 0.6, \ldots, 0.9$ cm^{-1}, whereas $\mu_s' = 9.7$ cm^{-1}. The scattering and absorption coefficients within the risk organs as well as the surrounding tissue were 8 and 0.3 cm^{-1}, respectively. Fig. 3.a shows the μ_{eff} evaluated from these data. Markers and error bars represent the average μ_{eff} and ± 1 standard deviation (SD), respectively, when averaging data for the 18 source fibers. The dashed line indicates the ideal fit to simulated data. The underestimation of the effective attenuation coefficient is probably caused by the lower overall attenuation within the remaining organs, especially influencing light transmission between fibers closer to either the urethra or the periphery of the prostatic gland. No such underestimation of μ_{eff} was evident for a totally homogeneous medium (data not shown). The Cimmino algorithm was used to predict the total irradiation times required were the light attenuation coefficient to remain at the levels given in Fig. 3.a

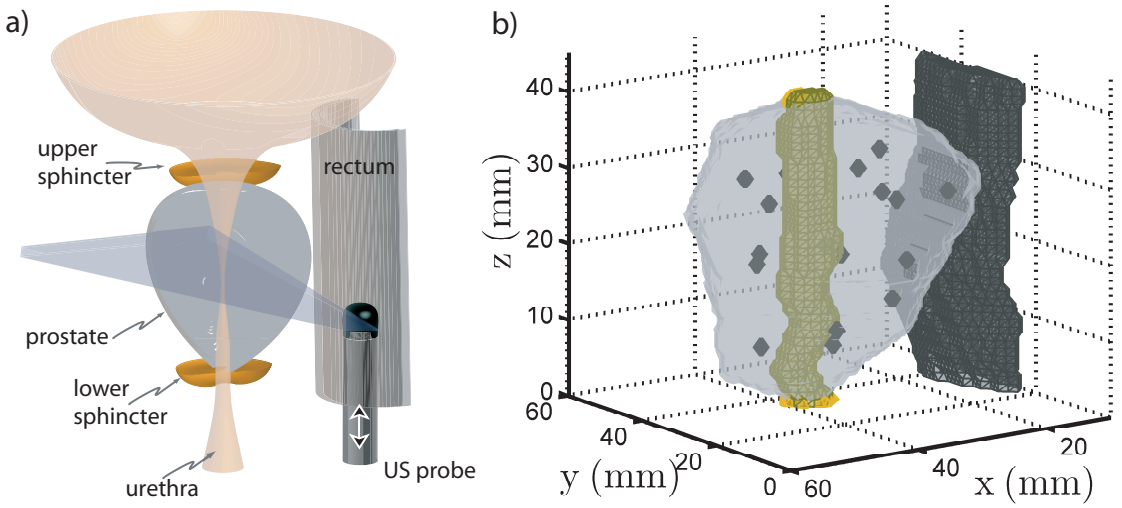

Figure 2. a) Illustration showing organs included in the geometry model. The ultrasound probe and one ultrasound cross-section are outlined as well. b) The geometry reconstructed from a set of 8 ultrasound images. The color coding is light grey for prostate, green for urethra, black for the rectal wall and yellow areas for the upper and lower sphincters. The calculated fiber positions are indicated by the dark grey markers.

during a full treatment. Fig. 3.b plots the required total light energy for these five levels of μ_{eff}, illustrating an increase in light energy, and thus total irradiation times, with higher overall absorption. Here, the connection between irradiation time and light dose is determined by a fiber output power of 0.15 W.

The first time the Cimmino algorithm (step 5) executes, no measurements have been performed and thus the default prostate optical properties are used when predicting fiber irradiation times, see Section 2.3. From this pre-treatment model, the estimated light dose distribution resulted in a DVH as illustrated by the solid black line in Fig. 4.a. As can be seen, 95% of the target volume was given a light dose exceeding the threshold. The realtime treatment dosimetry module (steps 6-9 in Fig. 1) was tested on a scenario with a treatment-induced increase in light attenuation. Simulated data on light transmission, see Section 2.5, were utilized to replace the *in vivo* measurements in step 6. Here, transmission data were simulated for $\mu_{\text{eff}} = 4.7$ cm^{-1} within prostate tissue. These light transmission signals were utilized as input for the *evaluation* module (step 8) for the first measurement sequence. The resulting data set thus represented an *in vivo* situation where the target tissue light attenuation was significantly higher than predicted by the pre-treatment model. μ_s' and μ_a within the sensitive organs remained at 8 and 0.3 cm^{-1}, respectively.

The calculated effective attenuation coefficients were identical to the last data point in Fig. 3.a. Following each execution of the *evaluation* module, the Cimmino algorithm was used to update individual fiber irradiation times. These two procedures were iterated until a sufficient light dose had been delivered to the target volume. The resulting DVHs for the delivered light dose and the individual fiber irradiation times were compared for the cases of no treatment feedback and treatment feedback based on the light transmission signals. In Fig. 4.a, the solid grey line indicates a significant under-treatment for the case of no treatment feedback. Only 75% of the target tissue receives a light dose exceeding the threshold dose. After enabling the treatment feedback, the resulting DVH again shows that 95% of the target tissue received a sufficient light dose. Fig. 4.b shows the prolonged irradiation times for the case of increased light attenuation and treatment feedback (white bars) as compared to the irradiation times predicted by the pre-treatment plan based on the default optical properties within the target tissue (black bars).

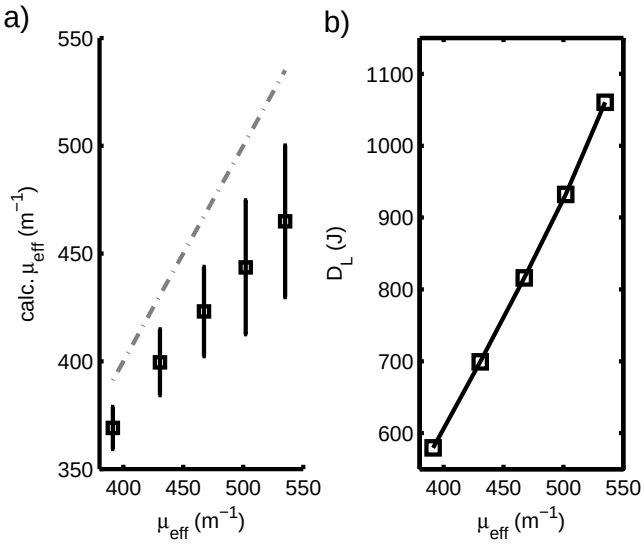

Figure 3. a) The average of the calculated $\mu_{\mathrm{eff}(i)}$ for different levels of absorption within prostate tissue. Data on light transmission were obtained from the FEM simulations. Error bars denote $\pm 1SD$ resulting when averaging the calculated $\mu_{\mathrm{eff}(i)}$ for the 18 treatment fibers. b) Total delivered light dose (D_L) as predicted by the Cimmino algorithm for the different attenuation coefficients.

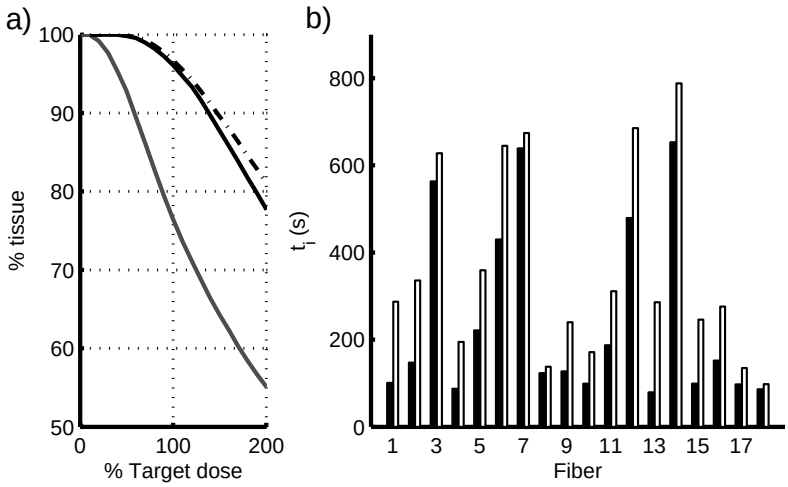

Figure 4. a) DVHs for the pre-treatment plan utilizing default prostate optical properties (black solid line), increased attenuation without treatment feedback (grey solid line) and with treatment feedback (black dash-dotted line). b) Individual fiber irradiation times for the pre-treatment plan (black bars) and for the case of increased attenuation with treatment feedback (white bars).

4. DISCUSSION

As IPDT on tissue is known to cause changes in light transmission and there exists a large biological variability of the prostate tissue composition, light doses required to treat the entire prostate gland are likely to vary between patients. We present a dosimetry model for IPDT on prostate tissue incorporating realtime treatment monitoring and treatment feedback. Algorithms have been implemented that utilize light transmission signals between treatment fibers in order to compensate the delivered light dose for any treatment-induced alterations of the light attenuation within the target tissue. The software consists of a pre-treatment and a realtime treatment

dosimetry module. The former starts by reconstructing the tissue geometry based on a number of ultrasound images of the treatment volume followed by a step optimizing the positions of a maximum of 18 treatment fibers within this volume. The pre-treatment dose plan, specifying individual fiber irradiation times, is created utilizing a set of default prostate optical properties and a Cimmino optimization algorithm. During the treatment procedure, the realtime dosimetry module then accepts input on the light transmission between the treatment fibers, repeatedly assessed during the course of the treatment. The method of spatially resolved spectroscopy is utilized to track the tissue effective attenuation coefficient. The measured coefficients are further fed into the Cimmino optimization algorithm to update individual fiber irradiation times, provided the requirements to deliver a pre-determined light dose to the target tissue while sparing surrounding, sensitive organs. By iterating the procedure of measuring the light transmission, evaluating the light attenuation and recalculating the required treatment time, a realtime treatment feedback based on the light dose threshold model is achieved. Furthermore, the light threshold dose of 5 J/cm^2 was found reasonable from the clinical work previously published by Bown *et al.*[13]

As a first step we tested the ability of the realtime treatment dosimetry module to detect an increasing effective attenuation coefficient, μ_{eff}, that was homogeneous within the prostate gland but different from surrounding organs. The FEM was utilized to model the diffuse light distribution within a realistic prostate model, providing the data on light transmission between treatment fibers that constitute the basis for the realtime dosimetry module. By employing spatially resolved spectroscopy, the *evaluation* module was able to track the homogeneous increase in tissue absorption, although the attenuation coefficient was consistently underestimated. This effect can possibly be explained by the fact that the detected photons also probed the urethra and surrounding tissue, characterized by lower levels of absorption and scattering. Based on the μ_{eff} calculated from the spatially resolved transmission signals, the Cimmino algorithm was utilized to predict the irradiation times required to treat the prostate gland while sparing the surrounding sensitive organs. Fig. 3.b illustrated the need to dramatically increase the total light dose for higher levels of light attenuation.

The ability of the realtime dosimetry module to detect and compensate changes to the effective attenuation coefficient occurring during the IPDT procedure was also investigated. The DVH from the pre-treatment model, utilizing a set of default optical properties, fulfilled the requirement of delivering a light dose exceeding the threshold dose within 95% of the target region, as illustrated in Fig. 4a. By utilizing the FEM simulations, the situation of an increased light absorption within the target tissue was modeled. For the case of no treatment feedback, a significant under-treatment of the target tissue could be noted. On the other hand, after enabling the realtime feedback, individual fiber irradiation times were adjusted so as to compensate the absorption increase. This feedback naturally resulted in increased irradiation time for most fibers, as shown in Fig. 4b. Here, we emphasize that the DVHs were calculated based on the evaluated optical properties. Due to the underestimation of μ_{eff}, the DVH based on the "true" light distribution would probably reflect some under-treatment.

During an *in vivo* treatment situation, tissue heterogeneities, such as calcifications, are likely to influence the light distribution. The current implementation, where spatially resolved spectroscopy is employed to assess the effective attenuation coefficient, is not able to localize such phenomena. Instead, the effects of tissue heterogeneities are averaged throughout the entire tissue volume probed by the transmitted light. A further challenge to the algorithm is local blood accumulation in front of the treatment fibers. Due to the strong absorption by hemoglobin, light transmission signals to and from occluded fibers will be characterized by poor SNR. The SNR threshold for including a transmission signal might be set to exclude fibers with large amounts of blood in front of the fiber tips. If ignoring data from one fiber, the algorithm instead includes more distant fibers when evaluating $\mu_{\text{eff}(i)}$, thereby averaging the level of light attenuation over larger volumes and making the procedure less sensitive to the presence of a few local heterogeneities. Extended simulations and *in vivo* clinical data will focus on this issue.

In this work, we have utilized a dosimetry model based on the light dose only. Although this simplified model is most often clinically used, extensive research has demonstrated the importance of also including parameters such as the sensitizer concentration and the tissue oxygenation within the target tissue.[22,23] At the moment, work is in progress to extend our realtime dosimetry model to incorporate these variables.

In conclusion, we have presented algorithms that constitute pre-treatment and realtime dosimetry modules for IPDT on the whole prostate glandular tissue. The software includes reconstruction of the target geometry,

optimization of source fiber positions within this geometry, monitoring of the light attenuation during the treatment procedure and updating individual fiber irradiation times to take into account any variation in tissue light transmission. We have shown that for increasing levels of light absorption, the requirements on the DVHs can still be fulfilled provided treatment feedback. On the other hand, a significant under-treatment was evident for the case of no treatment feedback.

5. ACKNOWLEDGEMENTS

SpectraCure AB (Lund, Sweden) is gratefully acknowledged for financial and technical support.

REFERENCES

1. R. Almeida, B. Manadas, A. Carvalho, and C. Duarte, "Intracellular signaling mechanisms in photodynamic therapy," *Biochimica et Biophysica Acta* **1704**(2), pp. 59–86, 2004.
2. M. Triesscheijn, M. Ruevekamp, M. Aalders, P. Baas, and F. Stewart, "Outcome of mTHPC mediated photodynamic therapy is primarily determined by the vascular response," *Photochem. Photobiol.* **81**(5), pp. 1161–1167, 2005.
3. F. van Duijnhoven, R. Aalbers, J. Rovers, O. Terpstra, and P. Kuppen, "Immunological aspects of photodynamic therapy of liver tumors in a rat model for colorectal cancer," *Photochem. Photobiol.* **78**(3), pp. 235–240, 2003.
4. J. Dysart, G. Singh, and M. Patterson, "Calculation of singlet oxygen dose from photosensitizer fluorescence and photobleaching during mTHPC photodynamic therapy of MLL cells," *Photochem. Photobiol.* **81**(1), pp. 196–205, 2005.
5. M. Patterson, B. Wilson, and R. Graff, "In vivo tests of the concept of photodynamic threshold dose in normal rat liver photosensitized by aluminum chlorosulphonated phthalocyanine," *Photochem. Photobiol.* **51**(3), pp. 343–349, 1990.
6. T. Farrell, B. Wilson, M. Patterson, and M. Olivo, "Comparison of the in vivo photodynamic threshold dose of photofrin, mono- and tetrasulfonated aluminum phthalocyanine using a rat liver model," *Photochem. Photobiol.* **68**(3), pp. 394–399, 1998.
7. T. Zhu, A. Dimofte, J. Finlay, D. Stripp, T. Busch, J. Miles, R. Whittington, S. Malkowicz, Z. Tochner, E. Glatstein, and S. Hahn, "Optical properties of human prostate at 732 nm measured in vivo during Motexafin Lutetium-mediated photodynamic therapy," *Photochem. Photobiol.* **81**(1), pp. 96–105, 2005.
8. R. Weersink, A. Bogaards, M. Gertner, S. Davidson, K. Zhang, G. Netchev, J. Trachtenberg, and B. Wilson, "Techniques for delivery and monitoring of TOOKAD (WST09)-mediated photodynamic therapy of the prostate: Clinical experience and practicalities," *J. Photochem. Photobiol. B* **79**(3), pp. 211–222, 2005.
9. T. Svensson, M. Einarsdottir, K. Svanberg, and S. Andersson-Engels, "In vivo optical characterization of human prostate tissue using near-infrared time-resolved spectroscopy," *in press J. Biomed. Opt.*, 2006.
10. A. Johansson, T. Johansson, M. Soto Thompson, N. Bendsoe, K. Svanberg, S. Svanberg, and S. Andersson-Engels, "In vivo measurement of parameters of dosimetric importance during photodynamic therapy of thick skin tumors," *J. Biomed. Opt.* **11**(3), 2006.
11. C. Moore, I. Hoh, S. Bown, and M. Emberton, "Does photodynamic therapy have the necessary attributes to become a future treatment for organ-confined prostate cancer?," *BJU International* **96**(6), pp. 754–758, 2005.
12. T. Nathan, D. Whitelaw, S. Chang, W. Lees, P. Ripley, H. Payne, L. Jones, M. Parkinson, M. Emberton, A. Gillams, A. Mundy, and S. Bown, "Photodynamic therapy for prostate cancer recurrence after radiotherapy: A Phase I study," *J. Urol.* **168**(4), pp. 1427–1432, 2002.
13. C. Moore, T. Nathan, W. Lees, C. Mosse, A. Freeman, M. Emberton, and S. Bown, "Photodynamic therapy using meso tetra hydroxy phenyl chlorin (mTHPC) in early prostate cancer," *Lasers Surg. Med.* bf 38(5), pp. 356–363, 2006.
14. J. Pinthus, A. Bogaards, R. Weersink, B. Wilson, and J. Trachtenberg, "Photodynamic therapy for urological malignancies: Past to current approaches," *J. Urol.* **175**(4), pp. 1201–1207, 2006.

15. K. Du, R. Mick, T. Busch, T. Zhu, J. Finlay, G. Yu, A. Yodh, S. Malkowicz, D. Smith, R. Whittington, D. Stripp, and S. Hahn, "Preliminary results of interstitial Motexafin Lutetium-mediated PDT for prostate cancer," *Lasers Surg. Med.* **38**(5), pp. 427–434, 2006.
16. M. Soto Thompson, A. Johansson, T. Johansson, S. Andersson-Engels, N. Bendsoe, K. Svanberg, and S. Svanberg, "Clinical system for interstitial photodynamic therapy with combined on-line dosimetry measurements," *Appl. Opt.* **44**(19), pp. 4023–4031, 2005.
17. A. Johansson, N. Bendsoe, K. Svanberg, S. Svanberg, and S. Andersson-Engels, "Influence of treatment-induced changes in tissue absorption on treatment volume during interstitial photodynamic therapy," *Med. Laser Appl.* **21**, pp. 261–270, 2006.
18. Y. Xiao, J. Galvin, M. Hossain, and R. Valicenti, "An optimized forward-planning technique for intensity modulated radiation therapy," *Med. Phys.* **27**(9), pp. 2093–2099, 2000.
19. M. Altschuler, T. Zhu, J. Li, and S. Hahn, "Optimized interstitial PDT prostate treatment planning with the Cimmino feasibility algorithm," *Med. Phys.* **32**(12), pp. 3524–3536, 2005.
20. Y. Censor, M. Altschuler, and W. Powlis, "On the use of Cimmino simultaneous projections method for computing a solution of the inverse problem in radiation-therapy treatment planning," *Inverse Problems* **4**(3), pp. 607–623, 1988.
21. G. Chen, "Dose volume histograms in treatment planning," *Int J. Radiat Oncol. Biol. Phys.* **14**(6), pp. 1319–1320, 1988.
22. B. Wilson, M. Patterson, and L. Lilge, "Implicit and explicit dosimetry in photodynamic therapy: a new paradigm," *Lasers Med. Sci.* **12**(3), pp. 182–199, 1997.
23. T. Zhu, J. Finlay, and S. Hahn, "Determination of the distribution of light, optical properties, drug concentration, and tissue oxygenation in-vivo in human prostate during Motexafin Lutetium-mediated photodynamic therapy," *J. Photochem. Photobiol. B* **79**(3), pp. 231–241, 2005.